Numerical Simulation of Rapid Expansion of Supercritical Carbon Dioxide

Jiewei Liu, Minh Do-Quang, and Gustav Amberg
Dept. of Mechanics, The Royal Institute of Technology, 100 44 Stockholm, Sweden

DOI 10.1002/aic.14603
Published online September 8, 2014 in Wiley Online Library (wileyonlinelibrary.com)

Axisymmetric rapid expansion of supercritical carbon dioxide is investigated in this article. The extended generalized Bender equation of state is used to give a good description of the fluids over a wide range of pressure and temperature conditions. The locations of Mach disks are analyzed and compared with an experimental correlation for the case where there is no plate positioned in front of the nozzle exit. It is found that the disagreement between our numerical results and the experimental formula is very small when the pressure ratio is small, and increases as the pressure ratio increases. It is also found that with different equations of state, the predicted positions of Mach disks do not differ a lot, but the temperature profiles in the chamber differ a lot. The case where there is a plate positioned in front of the nozzle exit is also studied in this article. A universal similarity solution is obtained. © 2014 American Institute of Chemical Engineers *AIChE J*, 61: 317–332, 2015

Keywords: rapid expansion, supercritical fluid, carbon dioxide, extended generalized Bender equation of state, Mach disk

Introduction

Rapid expansion of supercritical solutions (RESS) has received increased interest in recent years as a method to produce fine particles with very narrow particle-size distributions. This has been applied to pharmaceutical aerosols, pigments, surface coating, and so forth.[1–3] The solvating strength of supercritical fluids is directly related to the fluid density. Generally speaking, an increase in the density of the supercritical carbon dioxide results in higher solvent strength of carbon dioxide for various compounds.[4,5] During the expansion, the solvent transits from the supercritical state to the gaseous state or two-phase state very quickly, leading to a rapid drop in density and solvating strength. The combination of the rapid drop in density and very high supersaturation results in the formation of fine particles less than 1 μm.[1]

Carbon dioxide is the most commonly used supercritical solvent as it has several advantages.[6] First, its relatively low critical temperature (T_c=304.1282 K) and moderate critical pressure (p_c=7.3773 MPa) make its supercritical state easy to reach. Second, it is an environmentally friendly, nontoxic, low-cost, and widely available material. Third, it is in gaseous state under atmospheric condition, so the final product is solvent-free and has a high purity.

Experimental research on the RESS process has been conducted for over 20 years.[1] Numerical simulations serve as a good complementary tool to analyze and understand in-depth the fluid flow behavior. Although there are some published works in the literature on simulation of RESS, most of them are 1-dimensional (1-D). Two-dimensional and three-dimensional simulations of RESS are quite rare, to the authors' knowledge. A recent review of numerical investigations of supercritical fluid expansion is provided by Moussa and Ksibi.[2] There are numerous papers in the literature discussing 1-D numerical simulation of RESS, such as the series of papers of Türk and coworkers,[1,7–9] the series papers of Debenedetti and coworkers,[10–12] as well as other researchers like Lele and Shine,[13] Reverchon and Palado,[14] Weber and Thies,[15] and so forth. As our main focus is 2-D simulation, in the next two paragraphs, we review some 2-D results about the RESS process in the literature.

The first 2-D axisymmetric simulation of the supercritical fluid expansion was conducted by Ksibi et al.[16] The full Navier–Stokes equation and total energy equation with the Altunin and Gadestkii equation of state for carbon dioxide were solved by the Total Variation Diminishing scheme using finite difference method, with Roe averaged technique[17] for shock capturing. They studied the expansion of supercritical carbon dioxide into an expansion chamber which contained motionless pure carbon dioxide. Their studies focused on the profiles of thermodynamic variables along the centerline and the normal plate. Moussa et al.[18] carried out a parametric study on the nozzle geometry to control the supercritical fluid expansion for carbon dioxide using the same equations and numerical method as Ksibi et al.[16] did. Later, Moussa et al.[19] considered particle formation during the RESS process in their model. Particle transport and growth are governed by the time-dependent aerosol general dynamic equation (GDE). A lognormal size distribution function is assumed for the particles and the GDE is solved with a sectional method.

Franklin et al.[20] numerically simulated the RESS process for the perfluoropolyether-carbon dioxide supercritical

Correspondence concerning this article should be addressed to J. Liu at jiewei@mech.kth.se.

solution by solving the axisymmetric, Favre-averaged compressible Navier–Stokes equations with the lattice-fluid state equation of Sanchez and Lacombe. Separate continuity equations were used for air and carbon dioxide. Khalil and Miller[21] studied the structure of supercritical jet expansion for the inviscid, adiabatic pure carbon dioxide flow impacting on a flat plate. They solved an axisymmetric Euler equation with the Redlich–Kwong equation of state,[22] using a two-step Lax–Wendroff finite difference method. They showed that their numerical results compared reasonably well with their experiment if the pressure was not very high, and proposed that a divergent-convergent capillary seems to be more suitable for the RESS process than the convergent nozzles. Star and Edwards[23] studied the injection of supercritical ethylene into nitrogen, using the Peng–Robinson equation of state. Silvia et al.[24] investigated the growth of a magnetic thin film using carbon dioxide RESS expansion, following the work of Khalii and Miller[21] and Yamamoto et al.[25] studied the expansion of subcritical and supercritical carbon dioxide and water vapor, using the Altunin and Gadestkii equation of state. Later, Yamamoto et al.[26] simulated supercritical carbon dioxide flow across the critical point, and also briefly discussed rapid expansion.

When the supercritical fluid exits the nozzle exit, one of the typical characteristics is phase transition. The fluid transits from the supercritical state to a single-phase or two-phase state. All the models above have not considered the entropy and energy contribution from the two-phase interface. In 1893, van der Waals introduced a gradient term in the Helmholtz free energy density to describe a gas–liquid interface[27,28] for isothermal, one-component fluids. Such a gradient term began to be widely used thanks to the work of Cahn and Hilliard,[29] who studied the interfacial structure for isothermal, binary alloys by adding a gradient term to Helmholtz free energy. Later, Onuki[30] extended van der Waals theory to dynamic processes by considering that phase transitions, for a variety of situations, occur in flows with inhomogeneous temperature. His dynamic van der Waals theory was later adopted by other researchers to study their specific problems, such as the contact line motion in one component liquid–gas system[31] and boiling.[32] Considering the possible condensation of the fluid when it exits the nozzle, we are going to study the rapid expansion of supercritical carbon dioxide based on the dynamic van der Waals theory that was proposed by Onuki.[30]

It has been pointed out in literature,[7] that cubic equations of state, such as the van-der Waals (vdWs) or Peng–Robinson, failed to accurately estimate some properties of the fluid, and should be avoided in supercritical fluid calculations. Several researchers have demonstrated that the extended generalized Bender (egB) equation of state[33] could predict the fluid properties quite well even in the supercritical region.[8,16] In a series of papers, Türk and Helfgen et al.[1,8,9] studied the RESS process with the egB equation of state. However, their simulation is 1-D and only information along the centerline can be obtained. In this article, we are going to simulate the RESS process in the 2-D axisymmetric case with the egB equation of state. Some results calculated with the vdWs and the ideal gas equations of state will also be presented for comparison.

Another typical characteristic of the RESS process is the formation of shocks. When a high-pressure fluid exits from a nozzle to an ambient chamber with a much lower pressure, the free jet expands and decompresses very rapidly, leading to the formation of a strong shock called the Mach disk, which is normal to the flow direction. At the nozzle lip, an expansion fan forms. The expansion waves extending to the jet boundary are reflected back as compression waves, which coalesce to form the oblique shock in the interior of the jet.[34] Crist et al.[34] experimentally studied the underexpanded jet for various substances. An empirical formula was given which expressed the Mach disk location as a function only of the ratio of preexpansion pressure to expansion pressure $\frac{P_e}{P_0}$. Hatanaka and Saito found[35] that the geometry of the nozzle would indeed have an influence on the location of the Mach disk. They showed that when a cylindrical preexpansion chamber was connected with a cylindrical straight nozzle, if the radius ratio between them was larger than 4, the Mach disk location predicted from the ideal gas equation would be less than that given by Crist's experimental formula. We are going to study the Mach disk location when there is no plate positioned in front of the nozzle. We will show that the Mach disk locations predicted by our numerical simulations are very close to Crist's correlated formula when the pressure ratio is very small but will deviate from it as the pressure ratio increases. We will also show that with different equations of state, the positions of Mach disks do not differ a lot, but the temperature profiles in the outside chamber will.

When there was a plate positioned in front of the nozzle exit, through dimensional analysis, Fernandez de la Mora et al.[36] proposed a formula which correlated the Mach disk location to the pressure ratio as well as the position of the plate. Zare et al.[37] numerically studied the Mach disk location for airflow. They found that Fernandez de la Mora's formula was valid only if the plate was far from the nozzle exit. They extended Fernandez de la Mora's formula to include the case when the plate was close to the nozzle exit, by fitting their numerical results with a third order polynomial. We will show that our numerical simulations with the egB equation of state always fall on this curve, no matter where the plate is positioned or what the preexpansion pressure is.

The rest of this article is organized as follows: Section "Problem formulation" gives a short review of the dynamic van der Waals model and the egB equation of state. In "Numerical scheme" some specific techniques in the numerical solution of the equations are discussed briefly. The next section "Results and discussion" contains several subsections: the geometry of RESS process; numerical tests; temperature profiles calculated using different equations of state; Mach disk location with or without a plate positioned in front of the nozzle exit. The final section is conclusion.

Problem Formulation

Dynamic van der Waals model

The model we are going to use and modify in this article is the dynamic van der Waals model that has been used by Laurila et al.[32] to study boiling. The model, which was first proposed by Onuki,[30] is suitable for single component two phase flow simulations. A short review of this theory will be given in this section. In the following, variables with or without are dimensional and dimensionless, respectively.

In van der Waals theory, helmholtz free energy density for monoatomic molecules is considered as a function of density $\tilde{\rho}$ and temperature $\tilde{T}$[30]

$$\tilde{f}(\tilde{\rho},\tilde{T})=\frac{k_B\tilde{T}\tilde{\rho}}{m}\left[\ln\frac{\lambda_{th}^3\tilde{\rho}}{m-b\tilde{\rho}}-1\right]-a\left(\frac{\tilde{\rho}}{m}\right)^2 \tag{1}$$

where k_B is the Boltzmann constant, λ_{th} is the thermal de Broglie length with m being the molecular mass, $a=\epsilon b$ with ϵ being the magnitude of the attractive potential, b is the molecular volume. To describe an inhomogenous liquid–gas coexistence system, a gradient term is introduced in the Helmholtz free energy. Onuki[30] constructed a dynamic van der Waals model taking into account the gradient contribution to entropy and energy, respectively. Anderson et al.[38] have given a general principle to model such systems. The total mass $\tilde{\mathcal{M}}$, total momentum $\tilde{\mathcal{P}}$, total energy $\tilde{\mathcal{E}}$, and total entropy $\tilde{\mathcal{S}}$ are[30,38]

$$\tilde{\mathcal{M}}=\int_\Omega\tilde{\rho}dV \tag{2}$$

$$\tilde{\mathcal{P}}=\int_\Omega\tilde{\rho}\tilde{\mathbf{v}}dV \tag{3}$$

$$\tilde{\mathcal{E}}=\int_\Omega\left(\frac{1}{2}\tilde{\rho}\tilde{\mathbf{v}}^2+\tilde{e}+\frac{1}{2}K_e|\tilde{\nabla}\tilde{\rho}|^2\right)dV \tag{4}$$

$$\tilde{\mathcal{S}}=\int_\Omega\tilde{\rho}\tilde{s}-\frac{1}{2}K_s|\tilde{\nabla}\tilde{\rho}|^2dV \tag{5}$$

where $\tilde{\mathbf{v}}$ is the velocity, dV is the volume element, $\tilde{e}$ is the internal energy density, s is the entropy per unit mass, K_e, K_s are coefficients of the gradient terms in energy and entropy, respectively. Physical balance laws for mass, momentum, energy, and entropy can be expressed as[38] (body forces such as gravity are ignored)

$$\frac{d\tilde{\mathcal{M}}}{d\tilde{t}}=0 \tag{6}$$

$$\frac{d\tilde{\mathcal{P}}}{d\tilde{t}}=\int_{\partial\Omega}\tilde{\mathcal{F}}\cdot\hat{n}dA \tag{7}$$

$$\frac{d\tilde{\mathcal{E}}}{d\tilde{t}}=\int_{\partial\Omega}[\tilde{\mathbf{v}}\cdot\tilde{\mathcal{F}}\cdot\hat{n}-\tilde{q_E}\cdot\hat{n}]dA \tag{8}$$

$$\frac{d\tilde{\mathcal{S}}}{d\tilde{t}}-\int_{\partial\Omega}\tilde{q_s}\cdot\hat{n}dA=\int_\Omega\dot{s}^{\text{prod}}dV \tag{9}$$

$\tilde{\mathcal{F}}$ is stress tensor, $\tilde{q_E}$ is internal energy flux, $\tilde{q_s}$ is entropy flux, $\dot{s}^{\text{prod}}$ is the entropy production, $\hat{n}$ is outward unit normal vector, dA is surface element. Usually, $\tilde{\mathcal{F}}$, $\tilde{q_E}$, $\tilde{q_s}$ include both classical and nonclassical terms.[38] The exact form of $\tilde{\mathcal{F}}$, $\tilde{q_E}$, $\tilde{q_s}$ need to be determined by the second law of thermodynamics, that is, $\dot{s}^{\text{prod}}\geq 0$. Detailed derivations of those variables and the hydrodynamic equations can be found in literature.[30,31,38]

Onuki's generalized hydrodynamic equations are the following[30]:

density equation

$$\frac{\partial\tilde{\rho}}{\partial\tilde{t}}+\tilde{\nabla}\cdot(\tilde{\rho}\tilde{\mathbf{v}})=0 \tag{10}$$

momentum equation

$$\frac{\partial(\tilde{\rho}\tilde{\mathbf{v}})}{\partial\tilde{t}}+\tilde{\nabla}\cdot(\tilde{\rho}\tilde{\mathbf{v}}\tilde{\mathbf{v}})=-\tilde{\nabla}\cdot(\tilde{\tilde{\Pi}}-\tilde{\tilde{\sigma}})-\tilde{\rho}g\mathbf{e}_z \tag{11}$$

total energy equation

$$\frac{\partial\tilde{e_T}}{\partial\tilde{t}}+\tilde{\nabla}\cdot(\tilde{e_T}\tilde{\mathbf{v}})=-\tilde{\nabla}\cdot[(\tilde{\tilde{\Pi}}-\tilde{\tilde{\sigma}})\cdot\tilde{\mathbf{v}}]+\tilde{\nabla}\cdot(\tilde{\lambda}\tilde{\nabla}\tilde{T})-\rho g v_z \tag{12}$$

In the equations above

$$\tilde{\tilde{\Pi}}=\left(\tilde{p}-\frac{\kappa}{2}(\tilde{\nabla}\tilde{\rho})^2-\kappa\tilde{\rho}\tilde{\nabla}^2\tilde{\rho}\right)\hat{I}+\kappa\tilde{\nabla}\tilde{\rho}\tilde{\nabla}\tilde{\rho} \tag{13}$$

is the reversible stress tensor containing the gradient contribution from helmholtz free energy, κ is the coefficient of the gradient term and has the form of $\kappa=K_s\tilde{T}$.

$\tilde{p}$ is the thermodynamic pressure satisfying

$$\tilde{p}(\tilde{\rho},\tilde{T})=\tilde{\rho}\frac{\partial\tilde{f}(\tilde{\rho},\tilde{T})}{\partial\tilde{\rho}}-\tilde{f}(\tilde{\rho},\tilde{T})=\frac{k_B\tilde{T}\tilde{\rho}}{m-b\tilde{\rho}}-a\left(\frac{\tilde{\rho}}{m}\right)^2 \tag{14}$$

and

$$\tilde{\tilde{\sigma}}=\tilde{\mu}(\tilde{\nabla}\tilde{\mathbf{v}}+\tilde{\nabla}\tilde{\mathbf{v}}^{\perp})+(\tilde{\xi}-2\tilde{\mu}/3)\hat{I}\tilde{\nabla}\cdot\tilde{\mathbf{v}} \tag{15}$$

is the dissipative stress tensor, $\tilde{\xi}$ and $\tilde{\mu}$ are bulk and shear viscosity, respectively, and are assumed to be the same in this article.

As a function of $\tilde{\rho}$ and $\tilde{T}$, the internal energy $\tilde{e}$ is

$$\tilde{e}(\tilde{\rho},\tilde{T})=\tilde{f}(\tilde{\rho},\tilde{T})-\tilde{T}\frac{\partial\tilde{f}(\tilde{\rho},\tilde{T})}{\partial\tilde{T}}=\frac{3k_B\tilde{T}\tilde{\rho}}{2m}-\frac{a\tilde{\rho}^2}{m^2} \tag{16}$$

and total energy $\tilde{e_T}=\tilde{e}+0.5\tilde{\rho}\tilde{\mathbf{v}}^2$

Except in the neighborhood of the critical point, the transport coefficients, namely, the viscosity $\tilde{\mu}$ and heat conductivity $\tilde{\lambda}$ of liquid are much larger than those in gas.[30] For simplicity, following Onuki[30] and Laurila et al.,[32] we assume that they depend linearly on the density

$$\tilde{\mu}=\tilde{\mu_0}\tilde{\rho} \tag{17}$$

$$\tilde{\lambda}=\tilde{\lambda_0}\tilde{\rho} \tag{18}$$

The sound speed is calculated as[30]

$$\tilde{u}_s=\left(\frac{k_B\tilde{T}}{m}\right)^{1/2}\left(1+\frac{2}{3}-\frac{\tilde{T}_s}{\tilde{T}}\right) \tag{19}$$

where

$$\tilde{T}_s=2a\frac{\tilde{\rho}}{mk_B}\left(1-\frac{b\tilde{\rho}}{m}\right)^2 \tag{20}$$

is the spinodal temperature.

Notice that Eqs. 10–12 are written in conservative form which is important for shock capturing, since the primitive variables have large variations across the shock, while the flux variables have either zero or very small variations.[39]

The governing Eqs. 10–16 are nondimensionalized by introducing the following scaling

$$\tilde{\rho}=\rho^*\rho,\ \tilde{\mathbf{v}}=v^*\mathbf{v},\ \tilde{x}=L^*x,\tilde{z}=L^*z,\ \tilde{p}=p^*p,\ \tilde{T}=T^*T,\ \tilde{e}=p^*e \tag{21}$$

We choose (ρ^*,p^*,T^*) to be the critical point of the van der Waals fluid, so $\rho^*=\frac{m}{3b}$, $p^*=\frac{a}{27b^2}$, and $T^*=\frac{8a}{27k_Bb}$. We set $L^*=1\ \mu$m, which is the unit of nozzle diameter in our simulations. Characteristic velocity v^* is chosen to be the sound speed at the inlet for each simulations. After defining all the characteristic variables, the corresponding dimensionless equations are:

density equation

$$\frac{\partial\rho}{\partial t}+\nabla\cdot(\rho\mathbf{v})=0 \tag{22}$$

momentum equation

$$\frac{\partial(\rho\mathbf{v})}{\partial t}+\nabla\cdot(\rho\mathbf{v}\mathbf{v})=-R\nabla\cdot\hat{\Pi}+\frac{1}{\mathcal{R}e}\nabla\cdot\hat{\sigma}-GR\rho\mathbf{e}_z \tag{23}$$

total energy equation

$$\frac{\partial e_T}{\partial t}+\nabla\cdot(e_T\mathbf{v})=-\nabla\cdot[(\hat{\Pi}-\mathcal{R}e^{-1}R^{-1}\hat{\sigma})\cdot\mathbf{v}]+B\nabla\cdot(\rho\nabla T)-G\rho v_z \tag{24}$$

and

$$\hat{\Pi}=(p-\zeta T(\nabla\rho)^2-2\zeta T\rho\nabla^2\rho)\hat{I}+2\zeta T\nabla\rho\nabla\rho \tag{25}$$

$$\hat{\sigma}=\rho(\nabla\mathbf{v}+\nabla\mathbf{v}^{\perp})+\rho(1-\frac{2}{3})\hat{I}\nabla\cdot\mathbf{v} \tag{26}$$

For this system

$$p(\rho,T)=\frac{8T\rho}{3-\rho}-3\rho^2 \tag{27}$$

$$e(\rho,T)=\frac{4}{3}3T\rho-3\rho^2 \tag{28}$$

$$e_T=e+\frac{1}{2R}\rho\mathbf{v}^2 \tag{29}$$

Dimensionless parameters introduced are: Reynolds number $\mathcal{R}e=\frac{L^*v^*}{\mu_0}$, which measures the relative importance of inertial force to viscous force; the parameter $R=\frac{p^*}{\rho^*v^{*2}}=\frac{a}{9mbv^{*2}}$, which is proportional to the ratio of the attractive potential energy to the molecular kinetic energy,[31] the parameter $B=\frac{\tilde{\lambda}_0\rho^*T^*}{e^*v^*L^*}=\frac{8m\tilde{\lambda}_0}{3k_Bv^*L^*}$, the parameter $\zeta=\frac{CT^*\rho^{*2}}{2m^2p^*L^{*2}}$; and the normalized gravity acceleration $G=\frac{mgL^*}{a/9b}$.[30]

egB equation of state

As has been pointed out in the literature,[7] cubic equations of state may fail to accurately estimate the sound speed and residual part of the enthalpy, both for a pure substance and for a real mixture. To give a good prediction of the fluids over a wide range of pressure and temperature conditions, including the single-phase region, two-phase coexistence region as well as the supercritical region, an equation of state with some adjustable parameters is needed.[33] Several researchers have demonstrated that the egB equation of state[33] could predict the fluid properties quite well even in the supercritical region.[8,16] The equation of state for CO_2 that was developed by Span and Wagner[40] is considered to be the most accurate equation of state for CO_2, and the difference between the egB equation of state and Span and Wagner's equation of state is always less than 1.2%.[7]

In a series of papers,[7,8,41] Türk and coworkers studied the RESS-process using a steady-state 1-D fluid model to predict the thermodynamic properties of the pure solvent along the centerline, using egB equation of state. The shortcoming of those 1-D models is that they could not capture characteristics off-axis. In many applications, thermodynamic properties on the whole domain are needed, so 2-D studies of the flow are necessary. In this subsection, we are going to describe the egB equation of state which will be used in our calculations in later sections.

The egB equation of state is written as

$$\tilde{p}=\tilde{\rho}R_s\tilde{T}(1+\rho B_1+\rho^2B_2+\rho^3B_3+\rho^4B_4+\rho^5B_5+\rho^2(B_6+\rho^2B_7)\exp(-\rho^2)) \tag{30}$$

where $\rho=\tilde{\rho}/\rho_c$ is the dimensionless density. The coefficients $B_i=B_i(1/T,e_j)$ are functions of $1/T$ and e_j, $T=\tilde{T}/T_c$ is the dimensionless temperature, e_j are correlated with 95 general constants and two substance-specified parameters, the Pitzer factor and the Stiel factor.[33]

With the given equation of state (30), enthalpy, internal energy, heat capacity, and the sound speed can be determined as follows.[22]

The enthalpy per unit volume is calculated as (variables with underscore represent property per mole)

$$\tilde{h}(\tilde{T},\tilde{p})=\frac{1}{\underline{\tilde{V}}}\left[\underline{\tilde{h}}^{IG}(\tilde{T},\tilde{p})+R_u\tilde{T}(Z-1)+\int_{\underline{\tilde{V}}=\infty}^{\underline{\tilde{V}}=\underline{\tilde{V}}(\tilde{T},\tilde{p})}\left[\tilde{T}\left(\frac{\partial\tilde{p}}{\partial\tilde{T}}\right)_{\underline{\tilde{V}}}-\tilde{p}\right]d\underline{\tilde{V}}\right] \tag{31}$$

where $Z=\tilde{p}/\tilde{\rho}R_s\tilde{T}$ is the compressibility, R_s is the specific gas constant, R_u is the universal gas constant. Variables with superscript *IG* represent properties for ideal gas.

Internal energy density is

$$\tilde{e}(\tilde{T},\tilde{p})=\tilde{h}(\tilde{T},\tilde{p})-\tilde{p} \tag{32}$$

With Eqs. 30 and 32 for $\tilde{p}$ and $\tilde{e}$, replacing Eqs. 14 and 16, the simulations are performed using the egB equation of state.

The molar heat capacity at constant volume C_v is

$$\tilde{C}_v(\underline{\tilde{V}},\tilde{T})=\tilde{C}_v^{\,IG}(\underline{\tilde{V}},\tilde{T})+\tilde{T}\int_{\underline{\tilde{V}}=\infty}^{\underline{\tilde{V}}=\underline{\tilde{V}}(\tilde{T},\tilde{p})}\left(\frac{\partial^2\tilde{p}}{\partial\tilde{T}^2}\right)_{\underline{\tilde{V}}}d\underline{\tilde{V}} \tag{33}$$

The molar heat capacity at constant pressure $\tilde{C}_p$ is related to $\tilde{C}_v$ as follows

$$\tilde{C}_p(\underline{\tilde{V}},\tilde{T})=\tilde{C}_v(\underline{\tilde{V}},\tilde{T})+\frac{\tilde{T}}{\tilde{\rho}^2}M_w\left(\frac{\partial\tilde{p}}{\partial\tilde{T}}\right)_{\tilde{\rho}}^2\Big/\left(\frac{\partial\tilde{p}}{\partial\tilde{\rho}}\right)_{\tilde{T}} \tag{34}$$

M_w is the molar mass. With $\tilde{C}_p$, $\tilde{C}_v$, we can calculate sound speed as

$$\tilde{u}_s^2=\left(\frac{\tilde{C}_p}{\tilde{C}_v}\right)\left(\frac{\partial\tilde{p}}{\partial\tilde{\rho}}\right)_{\tilde{T}} \tag{35}$$

Using the same scaling to nondimensionalize equation of state (30)–(32), we obtain

$$p=\mathcal{C}\rho T(1+\rho B_1+\rho^2B_2+\rho^3B_3+\rho^4B_4+\rho^5B_5+\rho^2(B_6+\rho^2B_7)\exp(-\rho^2)) \tag{36}$$

$$e(T,p)=h(T,p)-p \tag{37}$$

dimensionless parameter $\mathcal{C}$ is defined as: $\mathcal{C}=\frac{R_s\rho^*T^*}{p^*}$.

Numerical Scheme

A finite element numerical toolbox femLego[42] has been used for all simulations. FemLego is a symbolic tool for solving partial differential equations. Users need to define all the equations, boundary conditions, initial conditions, and linear solvers in a single Maple sheet. A C and Fortran code will be generated automatically after compiling the Maple sheet.[43] In this article, variables are discretized in space with piece-wise linear base functions, linear systems are solved with the generalized minimal residual method (gmres), a first-order Euler forward scheme is used for time marching.

We apply the characteristic-based split (CBS) method[32] to solve Eqs. 22–26 using the vdWs equation of state (27)–(28) or the egB equation of state (36)–(37), in a cylindrical coordinate. More details about the CBS method can also be found in the book written by Zienkiewicz et al.[44] To simulate the RESS process during which axial and radial shocks are typical

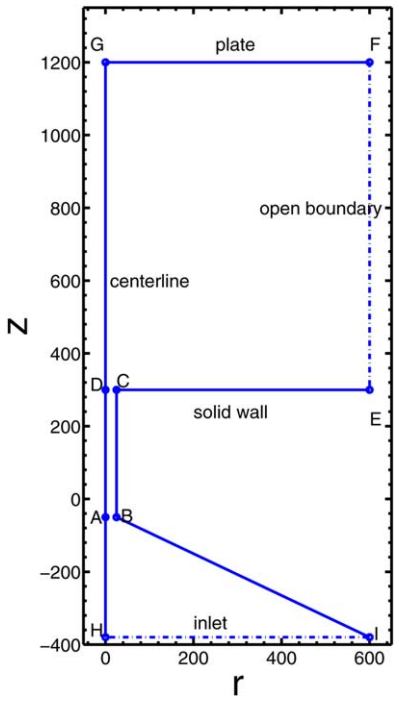

Figure 1. Dimensionless RESS geometry.

[Color figure can be viewed in the online issue, which is available at wileyonlinelibrary.com.]

characteristics, some numerical diffusion should be added to the scheme. We use the second derivative-based method[44,45] to damp out the oscillations caused by shocks and obtain as sharp a solution as possible. Numerical steps are the following (variables with a superscript n represent their values at time $n\triangle t$):

1. Solve Eq. 38 to obtain the intermediate mass flux $\mathbf{U}^*$

$$\frac{\mathbf{U}^*-\mathbf{U}^n}{\triangle t}=\left[-\nabla\cdot(\mathbf{U}\mathbf{v})-R\nabla\cdot\hat{\Pi}+\frac{1}{\mathcal{R}e}\nabla\cdot\hat{\sigma}-GR\rho\mathbf{e}_z\right]^n + \frac{\triangle t}{2}\mathbf{v}^n\cdot\nabla[\nabla\cdot(\mathbf{U}\mathbf{v})+R\nabla\cdot\hat{\Pi}+GR\rho\mathbf{e}_z]^n \tag{38}$$

2. Solve Eq. 39 to obtain pressure tensor at the new time step $\hat{\Pi}^{n+1}$

$$\hat{\Pi}^{n+1}=[(p(\rho,T)-\zeta T(\nabla\rho)^2-2\zeta T\rho\nabla^2\rho)\hat{I}+2\zeta T\nabla\rho\nabla\rho]^n \tag{39}$$

where $p(\rho,T)$ corresponds to Eq. 27 when using vdWs equation of state or Eq. 36 when using egB equation of state.

3. Solve Eq. 40 to obtain density at the new time step ρ^{n+1}

$$\frac{\rho^{n+1}-\rho^n}{\triangle t}=-\nabla\cdot[\mathbf{U}^n+\theta_1(\mathbf{U}^*-\mathbf{U}^n)-\theta_1\theta_2R\triangle t\nabla\cdot(\hat{\Pi}^{n+1}-\hat{\Pi}^n)] \tag{40}$$

4. Solve Eq. 41 to obtain total energy at the new time step T^{n+1}

$$\frac{e_T^{n+1}-e_T^n}{\triangle t}=[-\nabla\cdot(e_T\mathbf{v})-\nabla\cdot[(\hat{\Pi}-\mathcal{R}e^{-1}R^{-1}\hat{\sigma})\cdot\mathbf{v}] + B\nabla\cdot(\rho\nabla T)]^nG\rho v_z \tag{41}$$

where $e_T=e(\rho,T)$ and $e(\rho,T)$ corresponds to Eq. 28 when using vdWs equation of state or Eq. 37 when using egB equation of state.

5. Solve Eq. 42 to obtain mass flux at the new time step $\mathbf{U}^{n+1}$

$$\frac{\mathbf{U}^{n+1}-\mathbf{U}^*}{\triangle t}=-R\nabla\cdot(\theta_2(\hat{\Pi}^{n+1}-\hat{\Pi}^n)) + \frac{\triangle t}{2}\mathbf{v}^n\cdot\nabla[R\nabla\cdot(\theta_2(\hat{\Pi}^{n+1}-\hat{\Pi}^n))] \tag{42}$$

6. Solve temperature T^{n+1} from total energy e_T^{n+1}

7. Smoothing the solutions at the time step t^{n+1} by solving Eq. 43. Here, we use ϕ to represent any of the solution variables

$$\phi_s^{n+1}=\phi^{n+1}+\triangle tD(\phi^{n+1}) \tag{43}$$

where numerical diffusion is defined as[45]

$$D(\phi)=M_L^{-1}\sum_{\text{el}}\frac{C_{\text{el}}S_{\text{el}}}{\delta t_{\text{el}}}(M^{\text{el}}-M_{\text{L}}^{\text{el}})\phi^{\text{el}} \tag{44}$$

C_{el} is a user-specified coefficient, S_{el} is the element pressure switch calculated as a mean of nodal switches S_I

$$S_I=\frac{\{\sum_{\text{el}}(M^{\text{el}}-M_L^{\text{el}})p^{\text{el}}\}_I}{\{\sum_{\text{el}}|(M^{\text{el}}-M_L^{\text{el}}p^{\text{el}})|\}_I} \tag{45}$$

$$S_{\text{el}}=\frac{\sum_{I=1,\ldots,N_{\text{el}}}S_I}{N_{\text{el}}} \tag{46}$$

N_{el} is the number of vertex of a element, p is the thermodynamic pressure, and M, M_{L} are the consistent and lumped mass matrices, respectively, el represents the element.

Results and Discussion

Geometry

Figure 1 shows the geometry we use in this article. All calculations are made in axisymmetric geometry. *HIAB* is a convergent capillary inlet with a starting radius of L_{HI} and a length of L_{HA}. *ABCD* is a straight nozzle with a diameter of $d=2L_{AB}$ and a length of L_{AD}. *DCEFG* is an outside chamber. A plate *GF* is positioned at a distance of L_{DG} to the nozzle exit *CD*, *AB* is the straight nozzle inlet, *EF* is an open boundary, *CE* is a solid wall, and *HG* is the axisymmetric axis.

Numerical validations

Phase Separation. To check the capability of our model in describing phase transition process, we study the phase separation for a small domain by solving Eqs. 22–26 with the egB equation of state (36)–(37). Results are shown in Figure 2. The length scale is $L^*=1E-9$ m, and we use the sound speed at the critical point as characteristic velocity, so $v^*=174.984$ m/s. The dimensionless domain size is [0,250] $\times$ [300,550] with mesh resolution $l_c=2.5$.

Initially, the system has a uniform temperature $T=273.715$ K, uniform thermodynamic pressure $p=3.477$ MPa, and density $\rho=467.6$ kg/m^3 with random perturbation added, see Figure 2a. For egB equation of state, at $T=273.715$ K, densities of saturated vapor and liquid at equilibrium are: $\rho_{\text{g}}=98.5304$ kg/m^3, $\rho_{\text{l}}=920.3151$ kg/m^3. Figure 2b show that at $t=300$, the fluid has already decomposed to liquid and gas with the expected values of density,

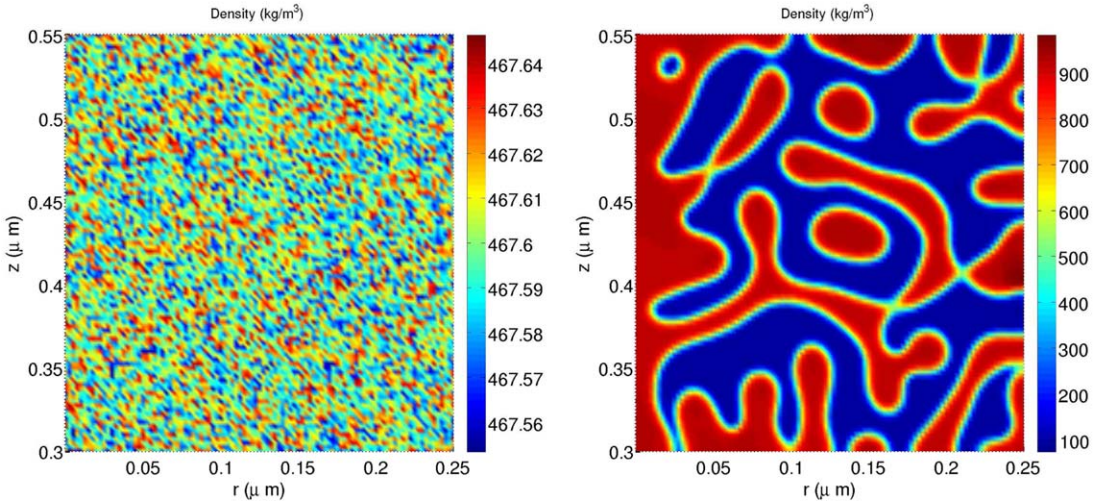

Figure 2. Phase separation with initial density ρ=467.6 kg/m^3, (a) $t=0$ and (b) $t=300$.

[Color figure can be viewed in the online issue, which is available at wileyonlinelibrary.com.]

so our model can capture phase transition and two-phase coexistence.

A Typical Run and Convergence Test. In this part, we run a typical case to study the jet expansion and show some convergence tests based on the vdWs equation of state. For simplicity, the computational domain does not include the convergent nozzle part *HIBA* in Figure 1. The geometric parameters are: diameter $d=2L_{AB}=50$ μm and length $L_{AD}=25$ μm, $L_{DG}=9.4d$. Pressure and temperature at inlet *AB* is: $\tilde{T}_i=332.65$ K, $\tilde{p}_i=7.535$ MPa, which gives $\tilde{\rho}_i=242.2761$ kg/m^3 through equation of state (14), and the sound speed $\tilde{u}_s=207.7486$ m/s according to (19)–(20). Atmospheric conditions are assumed in the large outside chamber: $\tilde{T}_o=293.15$ K, $\tilde{p}_o=0.101325$ MPa.

Initial distribution of temperature T and pressure p are the following

$$T(r,z,0)=\begin{cases} T_i, \text{if } z_A \le z \le z_D \\ T_o, \text{if } z_D \le z \le z_G \end{cases} \tag{47}$$

$$p(r,z,0)=\begin{cases} p_i+\dfrac{z-z_A}{z_D-z_A}(p_o-p_i), \text{if } z_A \le z \le z_D \\ p_o, \text{if } z_D \le z \le z_G \end{cases} \tag{48}$$

Initial distribution of $\rho(r,z,0)$ can then be obtained through equation of state (27).

Equations 22–28 are solved with the following boundary conditions:

1. At the inlet *AB*: $p=p_i$, $\rho=\rho_i$, $T=T_i$, $\mathbf{v}=u_s$, where u_s is the sound speed at the given inlet conditions.
2. At the plate *GF*: $\mathbf{v}=0$, $\frac{\partial\rho}{\partial n}=0$, $\frac{\partial T}{\partial n}=0$, $\frac{\partial p}{\partial n}=0$.
3. At the open boundary *EF*: atmospheric conditions for ρ, p, T.
4. At the solid wall *CE*: $\mathbf{v}=0$, ρ, p, T are fixed at atmospheric conditions.
5. At the nozzle wall *BC*: $\mathbf{v}=0$, $\frac{\partial\rho}{\partial n}=0$, $\frac{\partial T}{\partial n}=0$, $\frac{\partial p}{\partial n}=0$.
6. At the centerline *AG*: $\mathbf{v}\cdot\mathbf{n}=0$, $\frac{\partial\rho}{\partial n}=0$, $\frac{\partial T}{\partial n}=0$, $\frac{\partial p}{\partial n}=0$.

Table 1 shows the transport properties of carbon dioxide at $\tilde{T}=332.65$ K for $\tilde{p}=0.1$ MPa and $\tilde{p}=7.535$ MPa.[46] $\tilde{\mu}$ and $\tilde{\mu_0}$ are dynamic viscosity and kinematic viscosity, respectively, $\tilde{\lambda}$ is heat conductivity, $\tilde{\lambda_0}$ is heat conductivity per density. Average values of $\tilde{\mu_0}$ and $\tilde{\lambda_0}$ at the inlet and outside chamber are used to calculate the dimensionless parameter. The sound speed at the inlet is $v^*=207.7486$ m/s. With the scaling we defined previously,

all the dimensionless parameters related to this problem are: $\mathcal{R}e=70.7591$, $R=0.3655$, $B=0.3011$, $\zeta=2.9464E-6$, $G=0$.

Figure 3 shows profiles for density, temperature, thermodynamic pressure, and velocity magnitude at steady state. To see the rapid change of density and pressure in the chamber clearly, we plot the $\log_{10}$ function for these two variables. We can see that the Mach disk and barrel shock are well captured by our scheme. In the transition region from the nozzle exit to the shocks, temperature and pressure decrease rapidly, leading also to a rapid decrease in density. Outside the region bounded by the shocks, the thermodynamic variables increase due to the interaction with the atmosphere. The velocity profile is consistent with those thermodynamic variables. The velocity is increasing all the way until it reaches the Mach disk. At the Mach disk, the velocity decreases rapidly and the flow becomes subsonic. Although the temperature outside the nozzle decreases a lot, we have not observed any phase change. The continuous injection of carbon dioxide maintains the whole system in a nonequilibrium state. The fluid in the jet is in a rapid nonequilibrium flow, where simply there is no time to form liquid before conditions change.

To test the mesh convergence, we run this case on different meshes with characteristic mesh resolution l_c equal to 5, 2.5, and 1.25, respectively. Figure 4 shows density contours at

Table 1. Transport Properties of CO_2 at $\tilde{T}=332.65$ K

	$\tilde{p}=0.1$ (MPa)	$\tilde{p}=7.535$ (MPa)	Average Value
$\tilde{\rho}$ (kg/m^3)	2.510	242.2761	
$\tilde{\mu}$ (Pa·s)	1.955 E-5	1.4535 E-5	
$\tilde{\lambda}$ (W/(m·K))	2.9995 E-2	1.598 E-2	
$\tilde{\mu_0}$ (m^2/s)	8.07 E-8	5.79 E-6	2.936 E-6
$\tilde{\lambda_0}$ (m^2·W/(kg·K))	1.238 E-4	6.37 E-3	3.245 E-3

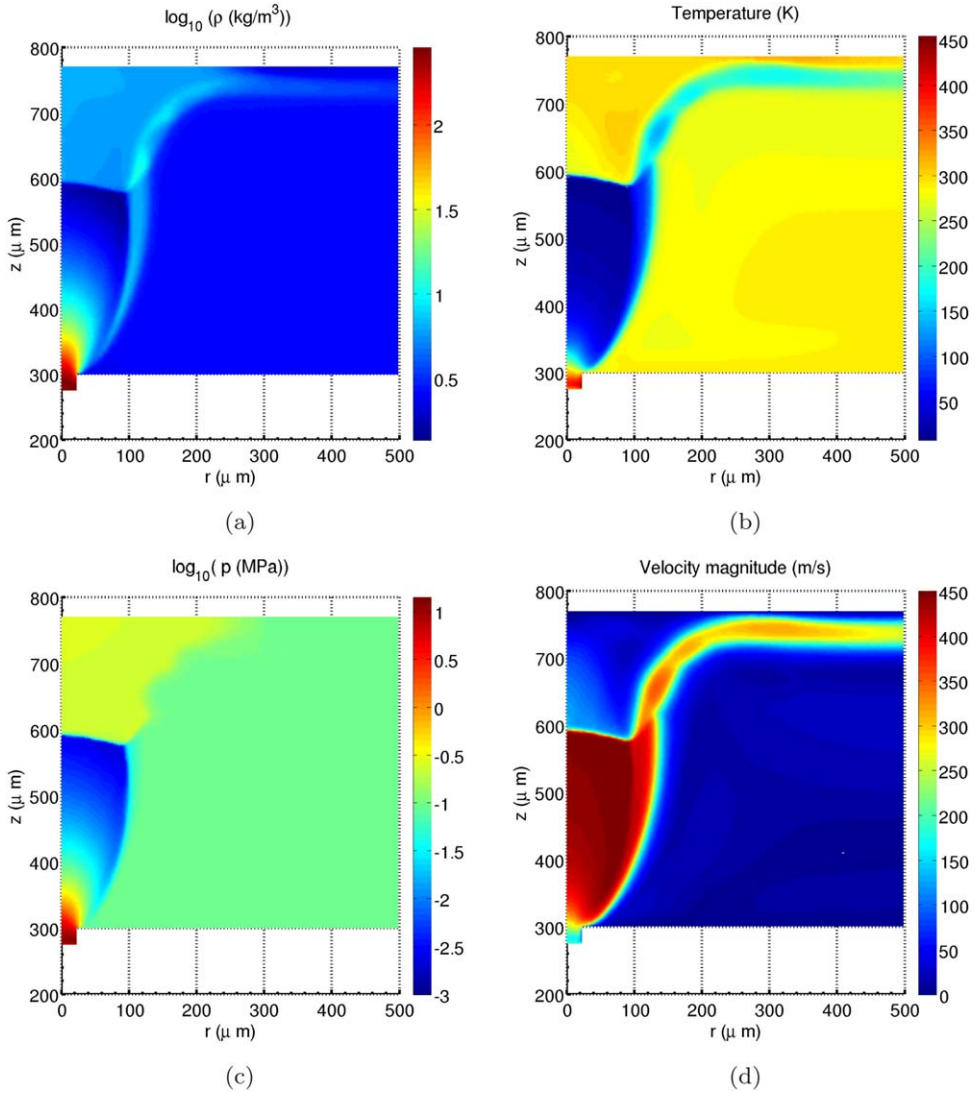

Figure 3. Profiles of (a) density $\log_{10}\rho$, (b) temperature T, (c) thermodynamic pressure $\log_{10}p$, and (d) velocity magnitude $\| v \|$ at steady state.

[Color figure can be viewed in the online issue, which is available at wileyonlinelibrary.com.]

$t = 1000$ for these three different meshes. It shows that as the mesh size decreases, shocks become sharper, and more detailed information about the shock structures can be seen. The position of the Mach disk are at $z = 600$ for all different mesh resolutions. The mesh with $l_c = 2.5$ is good enough to capture the core region of the supersonic jet, that is, the region bounded by the Mach disk and the oblique shock. It also tells us that solution on the finest mesh $l_c = 1.25$ should be able to be used as an approximation for the exact solution.

We then calculate the average L_2 norm for the density difference between two different meshes. The average L_2 norm on the whole computational domain Ω is defined as

$$E = \frac{\| \rho_{l_c}(r,z) - \rho_{l_c=1.25}(r,z) \|_{L_2}}{\int 1 d\Omega} = \frac{\int (\rho_{l_c}(r,z) - \rho_{l_c=1.25}(r,z))^2 d\Omega}{\int 1 d\Omega} \tag{49}$$

where $\rho_{l_c=1.25}(r,z)$ represents density on the mesh with $l_c = 1.25$ and $\rho_{l_c}(r,z)$ represents density on another mesh with mesh size l_c. We use unstructured meshes, where node points do not coincide for meshes with different resolutions, and we thus interpolate solutions of different meshes onto an identical mesh before calculating E in Eq. 49. The results are listed in Table 2. It shows that the average L_2 norm is very small and decreases as the mesh size decreases.

3-D Validation. In this part, we make a comparison between the 2-D axisymmetric simulation and a full 3-D simulation for flow in a small cylinder. The geometry, initial conditions and boundary conditions are the same as in section "A typical run and convergence test" above. Figure 5 shows our results at $t = 700$, using egB equation of state. It shows that the results predicted with 2-D and 3-D simulations are very good in comparison both qualitatively and quantitatively.

Temperature profiles with different EoS

It has been pointed out in literature[7] that the cubic equations of state, like the vdWs or the Peng–Robinson equation of state are able to give a good description of the vapor–liquid equilibrium and the phase behavior of dilute supercritical mixtures, yet they fail to accurately estimate the sound speed

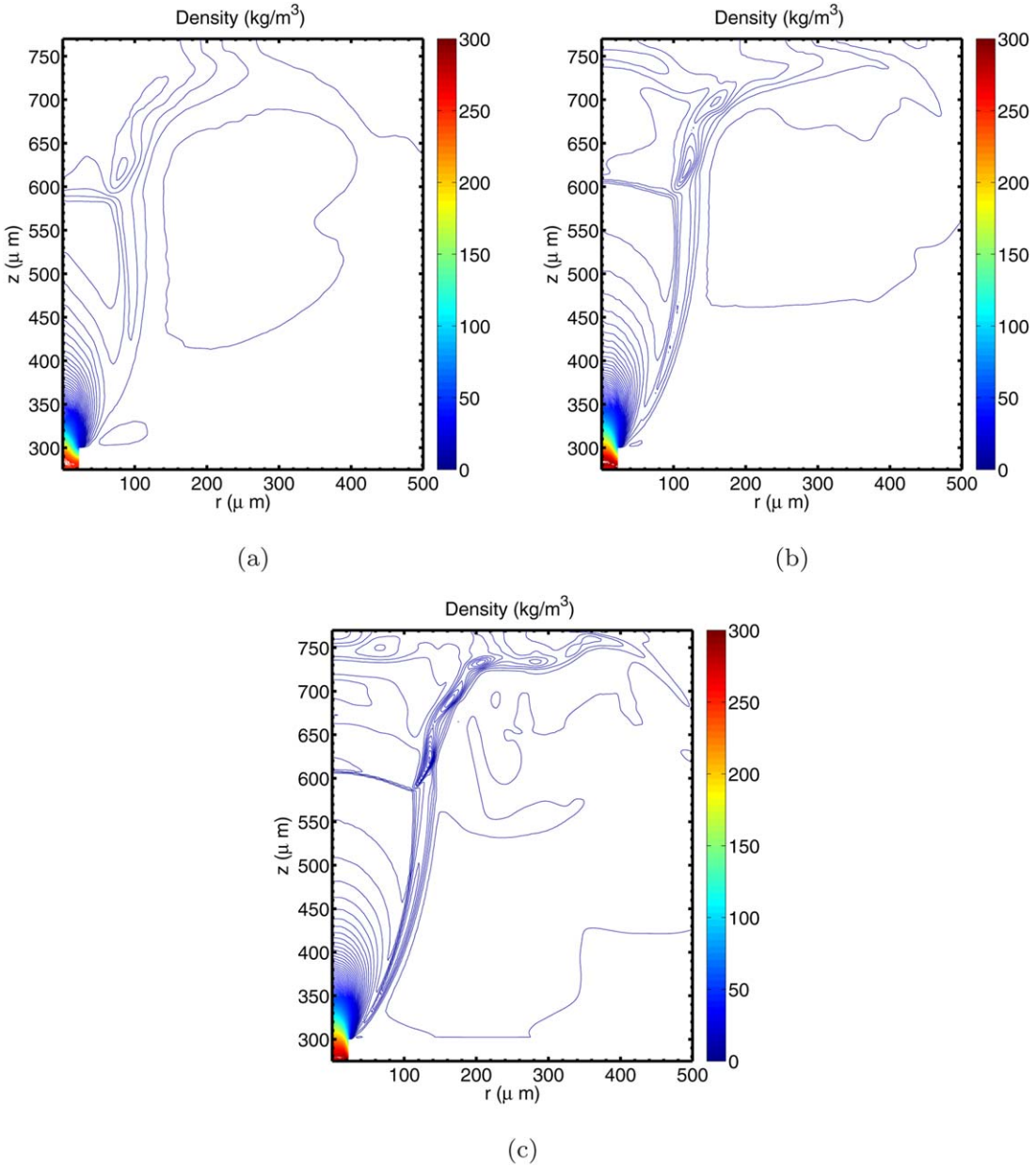

Figure 4. Density contours at $t = 1000$ for different meshes. (a) $l_c=5$, (b) $l_c=2.5$, and (c) $l_c=1.25$.

[Color figure can be viewed in the online issue, which is available at wileyonlinelibrary.com.]

and residual part of the enthalpy, both for a pure substance and for a real mixture.[7] To give a good prediction of the fluids over a wide range of pressure and temperature conditions, including the single-phase region, two-phase coexistence region as well as the supercritical region, an equation of state with some adjustable parameters is needed.[33] Although 1-D simulations, Türk,[7] Helfgen et al.[8] showed that the egB equation of state could describe the supercritical fluid very well. In this subsection, we are going to compare the temperature profiles obtained with different equations of state.

The geometric parameters we use in Figure 1 are: $L_{HI}=600$ μm, $L_{HA}=330$ μm, $d=2L_{AB}=60$ μm, $L_{AD}=350$ μm, $L_{DG}=9.4L_{AB}$. Initial conditions have the same expression as (47)–(48), but with z_A being replaced by z_H, and $\tilde{T}_i=\tilde{T}_e$, $\tilde{p}_i=\tilde{P}_e$. Boundary conditions are also the same as in section "A typical run and convergence test," the inlet boundary now is *HI* and velocity at the inlet is not specified. For the steep wall *BI*, we apply the same boundary condition as the nozzle wall *BC*.

Figure 6 shows the temperature T profiles along the centerline for three different equations of state: the egB equation of state (black squares), the van der Waals equation of state (blue circles), and the ideal gas law (red triangles). The pre-expansion condition is $\tilde{p}_e=13$ MPa, $\tilde{T}_e=388$K. It shows that both the vdWs equation of state and the ideal gas law predict an extremely low temperature, while the egB equation of state predict a higher temperature in the expansion chamber.

Table 2. Average L_2 Norm of the Error E

	$l_c=5$ vs. $l_c=1.25$	$l_c=2.5$ vs. $l_c=1.25$
E	4.256 e-3	2.485 e-3

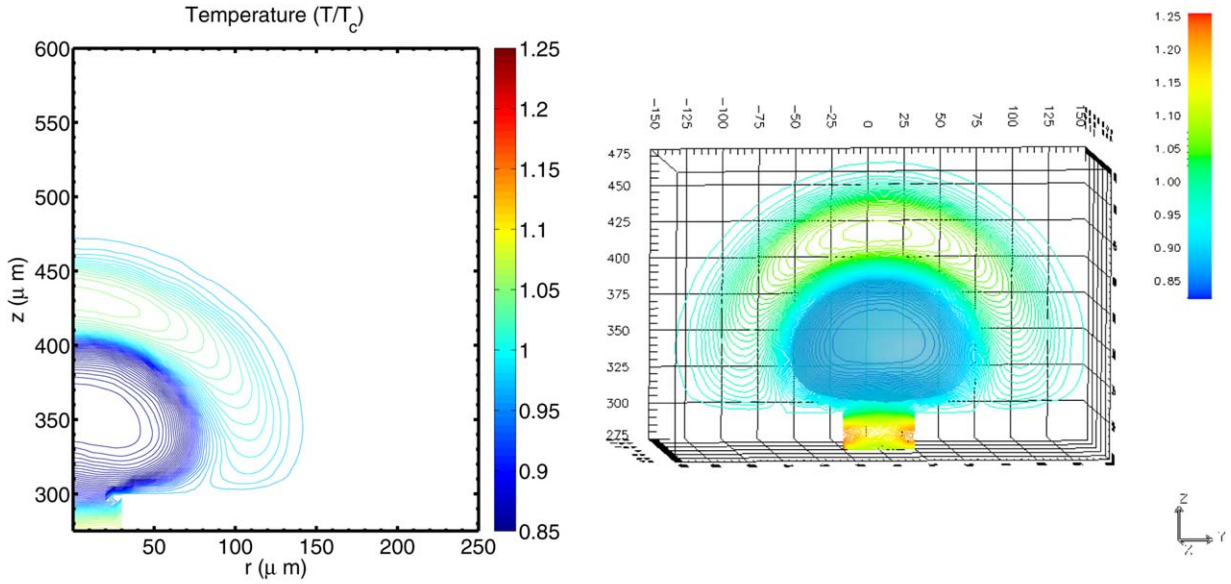

Figure 5. Profiles of dimensionless temperature T/T_c in (a) 2-D, (b) 3-D under preexpansion condition $\tilde{T}_e$=332.65 K, $\tilde{p}_e$=7.535 MPa, t = 700.

[Color figure can be viewed in the online issue, which is available at wileyonlinelibrary.com.]

The minimum temperature in the outside chamber is 12.5 K for the vdWs equation of state, and 180 K for the egB equation of state.

Mach disk location

In this section, we will investigate how the location of the Mach disk is determined by the different parameters. Referring to Figure 1, the geometrical parameters are: L_{HI}=600 μm, L_{HA}=330 μm, d=2L_{AB}=100 μm, L_{AD}=d= 100 μm. In subsection "Distance from Mach disk to nozzle exit without a plate," we set L_{DG}=6000 μm, and outflow boundary condition is applied there. In subsection "Distance from Mach disk to nozzle exit with a plate," we vary L_{DG} to study its effects on the jet and Mach disk location. Boundary conditions are the same as those used in subsection "Temperature profiles with different EoS."

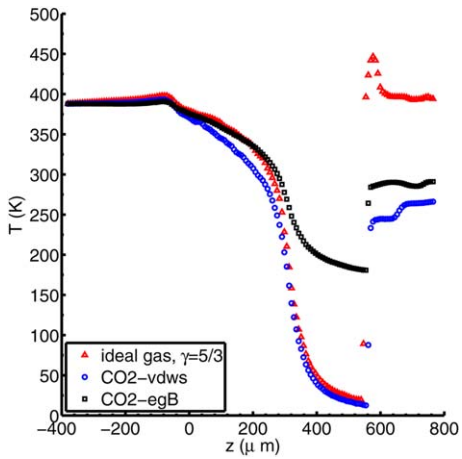

Figure 6. Profiles of temperature T along the centerline for three different EoS under preexpansion condition $\tilde{p}_e$=13 MPa, $\tilde{T}_e$=388K.

[Color figure can be viewed in the online issue, which is available at wileyonlinelibrary.com.]

Distance from Mach Disk to Nozzle Exit Without a Plate. Figure 7 shows the time evolution of the supersonic jet under preexpansion condition $\tilde{p}_e$=15 MPa, $\tilde{T}$=388 K. As seen in Figures 7a–d, the core region of the supersonic jet keeps developing. After t = 5000, the Mach disk stays at z = 1000, even though there is some development of the flow field also after this.

If we change the preexpansion pressure in Figure 7, the Mach disk location will also change. Crist et al.[34] experimentally studied the highly underexpanded jet for various substances. In their experiments, only nitrogen and helium were heated above 300°K, while the temperature of carbon dioxide was 298 K. They found that the Mach disk location was insensitive to nozzle lip geometry and specific heat ratio. The only parameter that did determine the Mach disk location was the ratio of preexpansion pressure to atmospheric pressure $\frac{P_e}{P_o}$. They expressed the dimensionless Mach disk location L_M/d as a function of $\frac{P_e}{P_o}$

$$\frac{L_M}{d}=0.65\sqrt{\frac{P_e}{P_o}} \tag{50}$$

Although Crist's formula did not show dependence of the size and location of the Mach disk on nozzle shape, Hatanaka and Saito found[35] that the geometry of the nozzle would indeed have an influence on them. They showed that when a cylindrical preexpansion chamber was connected with a cylindrical straight nozzle, if the radius ratio between them was larger than 4, the Mach disk location predicted from the ideal gas equations would be shorter than that given by Crist's experimental formula, and the deviation would become larger when the pressure ratio $\frac{P_e}{P_o}$ increased. At the maximum pressure ratio in their simulation, which was 40, the relative difference between $\frac{L_M}{D}$ determined from their simulation and Crist's formula was about 20%.

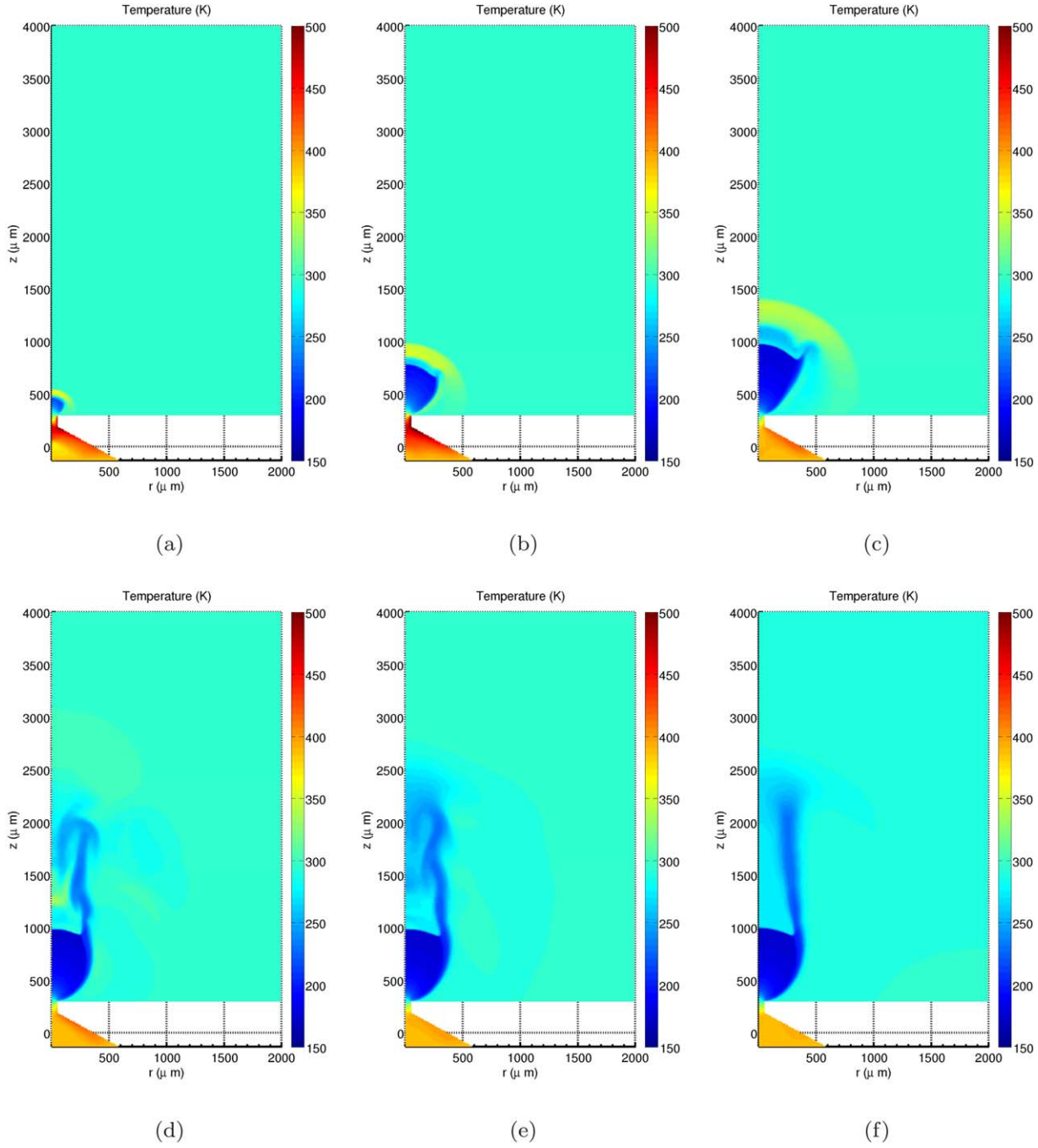

Figure 7. Time evolution of the temperature proflie for the supersonic jet under expansion condition $\tilde{p}_e$=15 MPa, $\tilde{T}_e$=388 K.

(a) t = 200, (b) t = 600, (c) t = 1000, (d) t = 5000, (e) t = 10,000, and (f) t = 20,000 (steady state). [Color figure can be viewed in the online issue, which is available at wileyonlinelibrary.com.]

We numerically study the Mach disk location using three different equations of state: egB equation of state, vdWs equation of state and the ideal gas law. Figure 8 shows the distance between the normal Mach disk and the nozzle exit at various pressure ratios $\frac{P_e}{P_o}$. The preexpansion temperatures are fixed at $\tilde{T}$=388 K or $\tilde{T}$=330 K. The atmospheric pressure $\tilde{P}_o$ is kept constant at 0.101325 MPa, while the preexpansion pressure $\tilde{P}_e$ is changed from 2.5 MPa to 40 MPa. For the van der Waal equation of state, the Mach disk only exists up to $\tilde{p}_e$=20 MPa when $\tilde{T}$=388 K and up to $\tilde{p}_e$=10 MPa when $\tilde{T}$=330 K. When we increase the preexpansion pressure beyond these values, the Mach disk disappears during the evolution, as seen in Figure 10. Figure 8 tells us that the equations of state indeed have a small influence on the calculated Mach disk location. Mach disk locations predicted with three different equations of state are very close to Crist's correlated formula when the pressure ratio is very small, but deviate from it as the pressure ratio increases. Similar results have been found by Hatanaka and Saito.[35]

Figure 9 are the temperature profiles calculated with different equations of state at t = 1000 and t = 20,000 under preexpansion condition $\tilde{p}_e$=12.5 MPa and $\tilde{T}_e$=388 K. The

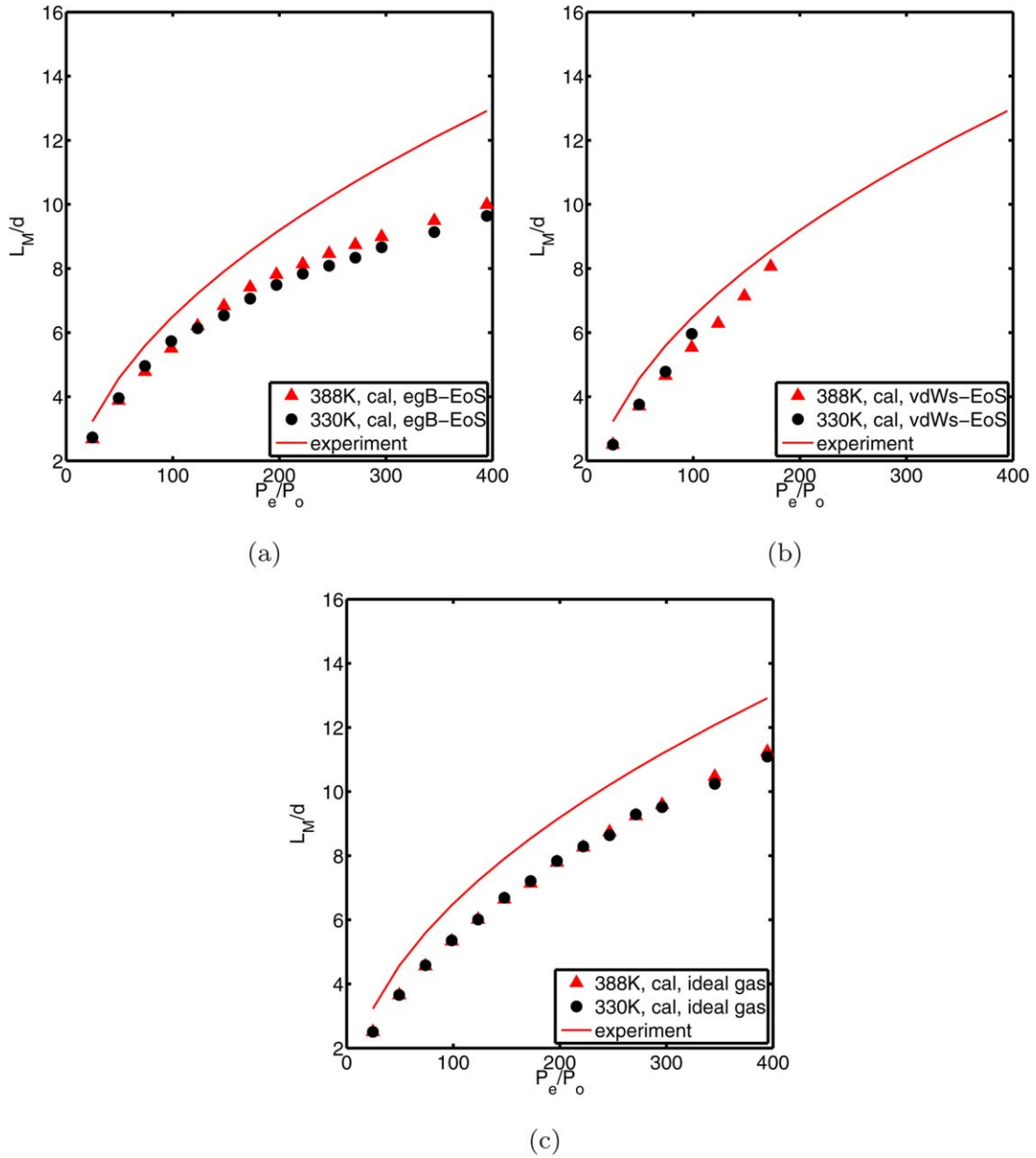

Figure 8. Distance of Mach disk to nozzle exit $\frac{L_M}{d}$ under different pressure ratio $\frac{P_e}{P_o}$ without a plate positioned in front of the nozzle.

(a) egB equation of state (EoS), (b) vdWs EoS, and (c) ideal gas law. [Color figure can be viewed in the online issue, which is available at wileyonlinelibrary.com.]

Mach disk and barrel shock are clearly seen at $t = 1000$. In later times, the Mach disk becomes narrow because of the compression of the barrel shock. The shape of the Mach disk and barrel shock are very similar when using the ideal gas law or vdWs equation of state, while the core region bounded by the Mach disk and the barrel shock are wider when using the egB equation of state.

Figure 10 are the temperature profiles calculated with different equations of state at $t = 1000$ (first row) and $t = 20{,}000$ (second row) under preexpansion condition $\tilde{p}_e = 22.5$ MPa and $\tilde{T}_e = 388$ K. The Mach disk and barrel shock are clearly seen at $t = 1000$. It shows that when $\frac{P_e}{P_o}$ increases, the core jet region calculated from van der Waals equation of state almost disappears at $t = 20{,}000$ and there is no Mach disk. Numerical tests with $\frac{P_e}{P_o} > 22.5$ also have been done, results are even worse than 10 (b). Those computation results indicate that van der Waals equation of state is not suitable for RESS calculations if preexpansion pressure is too high.

Distance from Mach Disk to Nozzle Exit with a Plate. In many applications, like the inertial impaction or coating, a plate will be positioned in front of the nozzle exit to collect particles and produce special surfaces. An investigation of the effect of a plate on the flow field and Mach disk location is important for such processes. With a plate positioned perpendicularly to the jet at a distance of L_p from the nozzle exit, the Mach disk becomes a bow shock wave, which interacts with the jet centerline at a distance δ upstream from the plate.[37]

Figure 11 shows the time evolution of the supersonic jet under preexpansion conditions $\tilde{p}_e = 15$ MPa, $\tilde{T} = 388$ K,

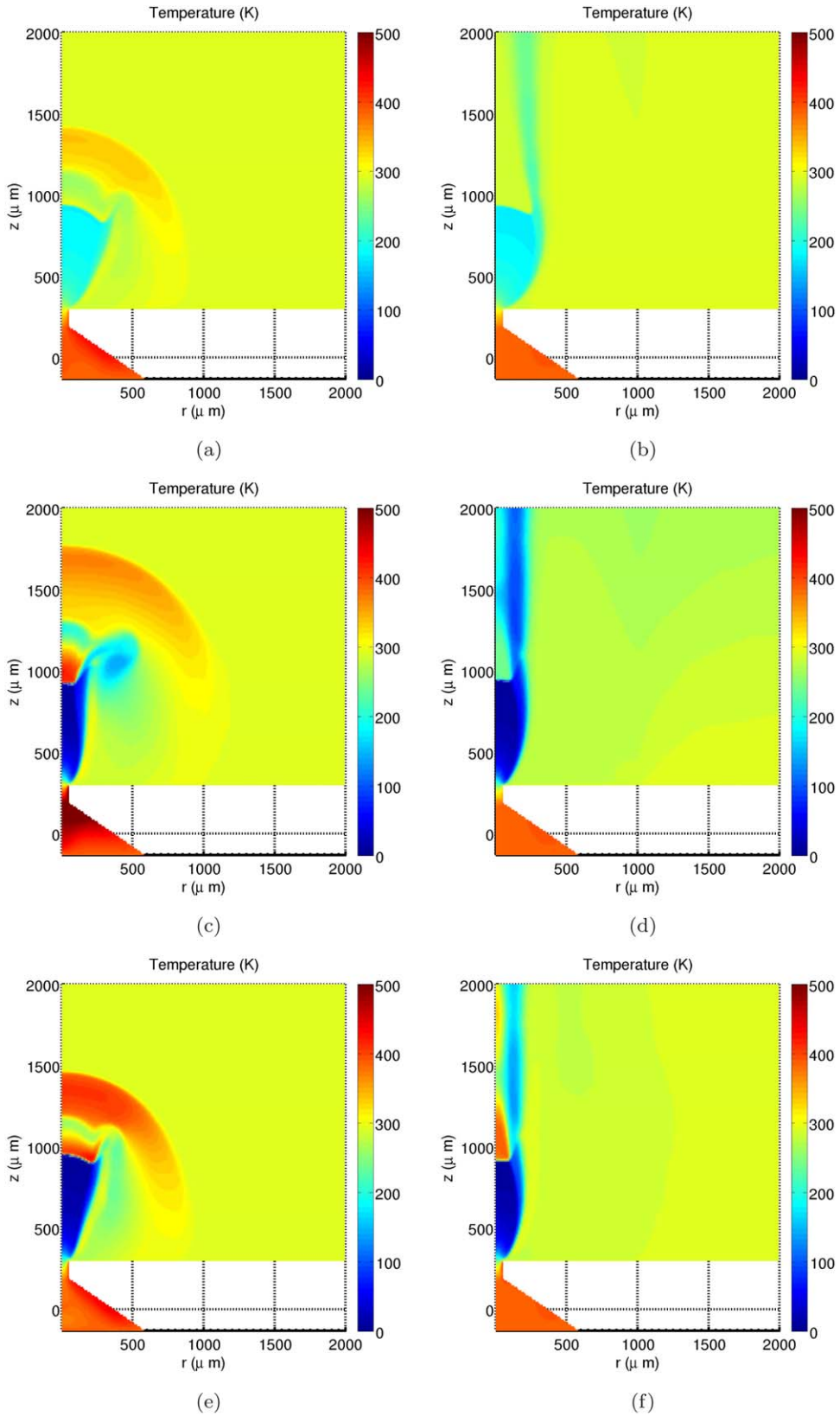

Figure 9. Profiles of temperature T under expansion condition $\tilde{T}_e$=388 K, $\tilde{p}_e$=12.5 MPa.

(a and b) egB-EoS, (c and d) vdWs-EoS, (e and f) ideal gas law. Left column: t=1000, right column: t = 20,000. [Color figure can be viewed in the online issue, which is available at wileyonlinelibrary.com.]

when there is a plate positioned in front of the nozzle at a distance of L_p=5d. We can see that the presence of a plate constrains the development of the supersonic jet in the z direction, and makes it expand more in the r direction, and the flow is also forced to change its direction abruptly.

Through dimensional analysis, Fernandez de la Mora et al.[36] proposed the following correlation

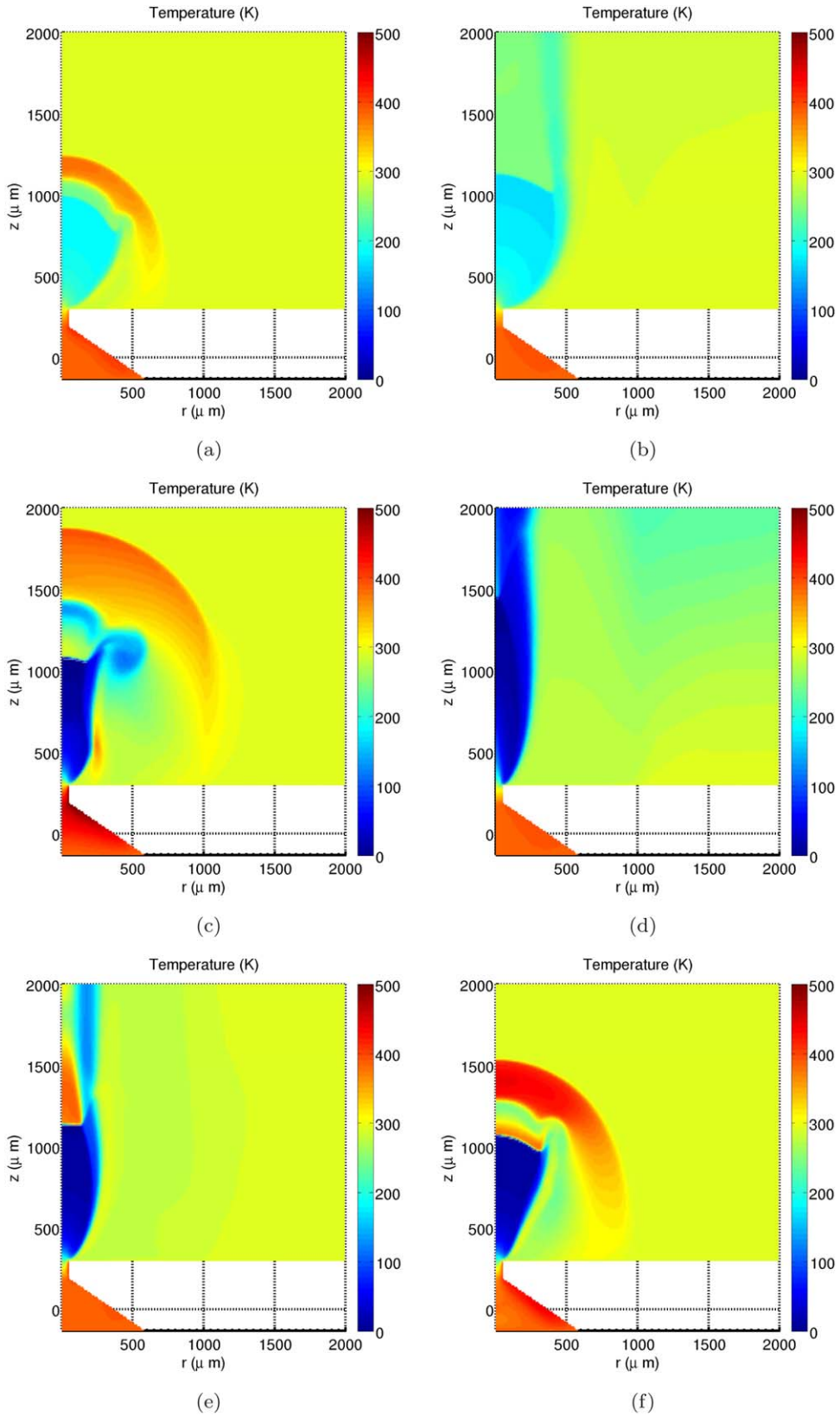

Figure 10. Profiles of temperature T under expansion condition $\tilde{T}_e$=388 K, $\tilde{p}_e$=22.5 MPa.

(a and b) egB-EoS, (c and d) vdWs-EoS, (e and f) ideal gas law. Left column: t=1000, right column: t = 20,000. [Color figure can be viewed in the online issue, which is available at wileyonlinelibrary.com.]

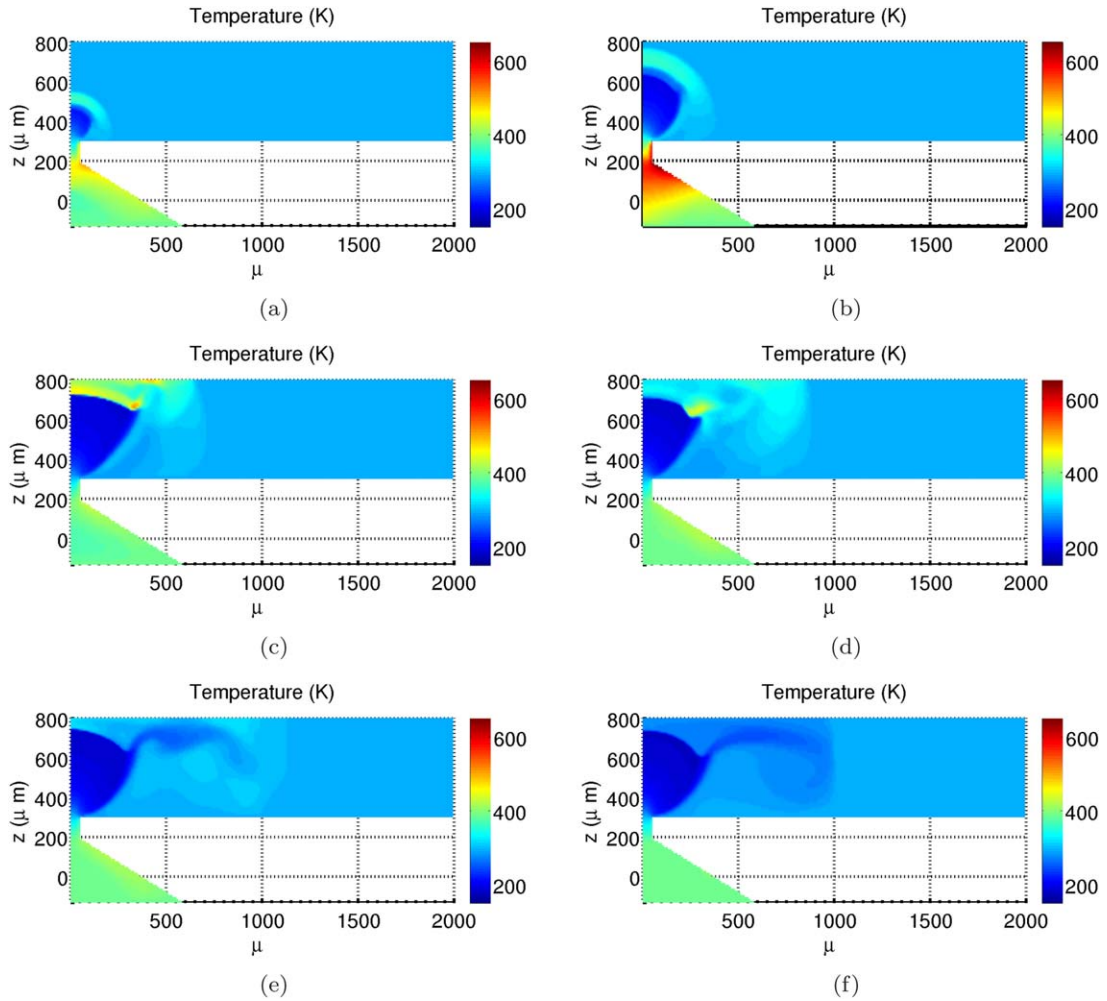

Figure 11. Time evolution of the temperature proflie for the supersonic jet under expansion condition $\tilde{p}_e$=15 MPa, $\tilde{T}_e$=388 K, L_p=10d.

(a) t = 200, (b) t = 400, (c) t = 800, (d) t = 1000, (e) t = 5000, and (f) t = 20,000. [Color figure can be viewed in the online issue, which is available at wileyonlinelibrary.com.]

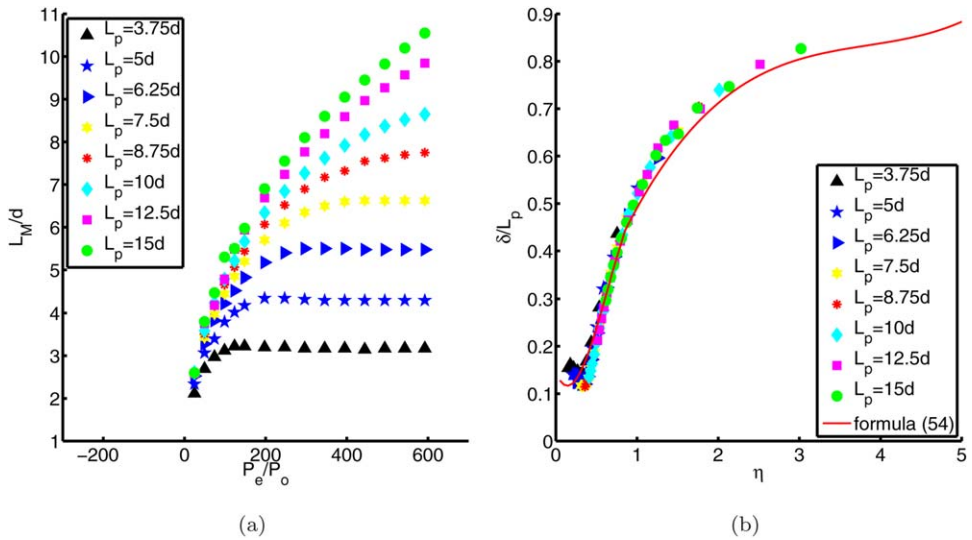

Figure 12. (a) The distance between the Mach disk and nozzle exit $\frac{L_M}{d}$ as a function of pressure ratio $\frac{P_e}{P_o}$ for different L_p, (b) The distance between the Mach disk and the plate $\frac{\delta}{L_p}$ as a function of η for different L_p.

[Color figure can be viewed in the online issue, which is available at wileyonlinelibrary.com.]

$$\frac{\delta}{L_p} = F(\eta) \tag{51}$$

where

$$\eta = \frac{L_p}{d} \Big/ \sqrt{\frac{P_e}{P_o}} \tag{52}$$

It is reasonable to expect that formula (51) will be consistent with formula (50) when $L_p/L_M \gg 1$, since the plate should not affect the shock position in this case. Rewriting formula (50) in the form of formula (51), we obtain

$$F(\eta) = 1 - 0.65/\eta, \quad \text{when} \quad \eta \gg 1 \tag{53}$$

Fernandez de la Mora et al.[36] use 0.67 in formula (53).

Zare et al.[37] studied the relationship between $\frac{\delta}{L_p}$ and $F(\eta)$ for airflow when there was a plate positioned in front of the nozzle exit. They found that formula (53) was not valid for small η. In their study, the preexpansion conditions were $\tilde{p}_e = 0.101325$ MPa, $\tilde{T}_e = 300$ K, and a typical pressure ratio $\frac{P_e}{P_o} = 400$ was used. Based on their numerical results, a new correlation[37] between $\frac{\delta}{L_p}$ and $F(\eta)$ has been proposed as follows,

$$\frac{\delta}{L_p} = F(\eta) = \begin{cases} -0.8743\eta^3 + 1.6322\eta^2 - 0.4108\eta + 0.1445, \text{if } 0.05 \le \eta \le 0.85 \\ 0.0117\eta^3 - 0.1346\eta^2 + 0.5413\eta + 0.0703, \text{if } 0.85 < \eta \le 5 \\ 1 - 0.67/\eta, \text{if } \eta > 5 \end{cases} \tag{54}$$

We solve Eqs. 22–26 with egB equation of state (36)–(37). The plate position L_p changes from 3.75 d to 15 d. For each specific L_p, we change the pressure ratio $\frac{P_e}{P_o}$ to obtain different values of η. Figure 12 shows the distance between (a) the Mach disk and nozzle exit $\frac{L_M}{d}$, (b) the Mach disk and the plate $\frac{\delta}{L_p}$, as a function of pressure ratio $\frac{P_e}{P_o}$ for different L_p. Figure 12a tells us that an increase in pressure ratio $\frac{P_e}{P_o}$ will lead to an increase in $\frac{L_M}{d}$. However, if the plate is close enough to the nozzle exit, there is a critical pressure ratio $(\frac{P_e}{P_o})_c$ at which $\frac{L_M}{d}$ reaches a maximum. When $\frac{P_e}{P_o} > (\frac{P_e}{P_o})_c$, a further increase in pressure ratio $\frac{P_e}{P_o}$ will not influence the Mach disk location any more. Figure 12b compares our results with the formula (54). It shows that, although different L_p and $\frac{P_e}{P_o}$ result in different $\frac{L_M}{d}$, yet when we rescale the variables using formula (52), all cases show similar behavior and fall on the same curve as is proposed by the previous study.

Conclusion

This article has studied the axisymmetric rapid expansion of supercritical carbon dioxide, based on a modified thermodynamic model. The whole system is solved with the CBS method. Artificial diffusion is added to the scheme to damp out the oscillations caused by the shocks.

It has been pointed out in previous studies that the cubic equations of state is not suitable for supercritical fluid calculations. It is shown in this article that the temperature calculated with the vdWs equation of state for supercritical fluid is extremely low. The new model which replaces the vdWs equation of state by the egB equation of state, shows a much more reasonable higher temperature profile in the outside chamber.

The formation of shocks is a typical characteristic of the RESS process and information of the Mach disk location is important for many applications. Based on the egB model, we have studied Mach disk location when there is no plate placed in front of the nozzle exit. Results with vdWs equation of state and ideal gas law are also presented for comparison. It is found that the Mach disk locations predicted by our numerical simulations are very close to Crist's correlated formula when the pressure ratio is very small, but deviate from it as the pressure ratio increases. We also show that the positions of Mach disks do not change very much between the different equations of state, but the temperature profiles in the outside chamber differ a lot.

We also studied the case when there is a plate placed in front of the nozzle exit at different distances, for egB equation of state. The ratio of the distance from the Mach disk to the plate δ and the distance from the nozzle exit to the plate L_p is influenced by both the pressure ratio $\frac{P_e}{P_o}$ and L_p: $\frac{\delta}{L_p} = F(\eta)$, where $\eta = \frac{L_p}{d} / \sqrt{\frac{P_e}{P_o}}$. Similarity solutions are obtained for different pressure ratio $\frac{P_e}{P_o}$ and L_p. It is also found that for each plate position, when $\frac{P_e}{P_o}$ is relatively small, an increase in $\frac{P_e}{P_o}$ makes the Mach disk move forward toward the plate. But with L_p small enough, there is a critical pressure ratio $(\frac{P_e}{P_o})_c$ at which the distance between the Mach disk and the nozzle exit L_M stays almost constant. A further increase in pressure ratio $\frac{P_e}{P_o}$ has no effect on L_M.

Acknowledgments

We appreciate Prof. Klas Hjort, Prof. Charlotta Turner and Researcher Irene Rodriguez Meizoso a lot, for inspiring and interesting discussions about this topic. We are also grateful to Professor Xu Kun, for the detailed discussions about energy equations in describing flow with shocks. Our thanks also goes to Dr. Xinpeng Xu, who contributed many discussions about the dynamic van der Waals model. Computer time was provided by the Swedish National Infrastructure for Computing SNIC. Support by the Swedish Research Council VR (2011-5037) is gratefully acknowledged.

Literature Cited

1. Türk M. Influence of thermodynamic behaviour and solute properties on homogeneous nucleation in supercritical solutions. *J Aerosol Sci*. 2001;32:295–319.
2. Moussa AB, Ksibi H. A review of numerical investigations regarding the supercritical fluid expansion in the RESS process. *Int J Emerging Multidisciplinary Fluid Sci*. 2010;2:45–58.
3. Werner O, Turner C. Investigation of different particle sizes on superhydrophobic surfaces made by rapid expansion of supercritical solution with in situ laser diffraction (RESS-LD). *J Supercrit Fluids*. 2012;67:53–59.
4. Dean JR. *Applications of Supercritical Fluids in Industrial Analysis*. Springer, USA, Canda: CRC Press, Inc., 1993.
5. Jia M. Particle formation in supercritical carbon dioxide by the RESS process. Master Thesis. London: The University of Western Ontario, 2003.
6. Chernyak Y, Henon F, Harris RB, Gould RD, Franklin RK, Edwards JR, DeSimone JM, Carbonell RG. Formation of perfluoropolyether coatings by the rapid expansion of supercritical solutions (RESS) process. Part 1: experimental Results. *Ind Eng Chem Res*. 2001;40:6118–6126.
7. Türk M. Formation of small organic particles by RESS: experimental and theoretical investigations. *J Supercrit Fluids*. 1999;15:79–89.
8. Helfgen B, Hils P, Holzknecht C, Türk M, Schaber K. Simulation of particle formation during the rapid expansion of supercritical solutions. *J Aerosol Sci*. 2001;32:295–319.

9. Helfgen B, Türk M, Schaber K. Hydrodynamic and aerosol modelling of the rapid expansion of supercritical solutions (RESS-process). *J Supercrit Fluids*. 2003;26:225–242.
10. Tom JW, Debenedetti PG. Particle formation with supercritical fluids—a review. *J Aerosol Sci*. 1991;22:555–584.
11. Kwauk X, Debenedetti PG. Mathematicalmodeling of aerosolformation by rapid expansion of supercritical solutions in a converging nozzle. *J Aerosol Sci*. 1993;24:445–469.
12. Debenedetti PG, Tom JW, Kwauk X, Yeo S-D. Rapid expansion of supercritical solutions (RESS): fundamentals and applications. *Fluid Phase Equilib*. 1993;82:311–321.
13. Lele AK, Shine AD. Morphology of polymers precipitated from a supercritical solvent. *AIChE J*. 1992;38:742–752.
14. Reverchon E, Pallado P. Hydrodynamic modeling of the RESS process. *J Supercrit Fluids*. 1995;8:318–328.
15. Weber M, Thies MC. A simplified and generalized model for the rapid expansion of supercritical solutions. *J Supercrit Fluids*. 2007; 40:402–419.
16. Ksibi H, Tenaud C, Subra P, Garrabos Y. Numerical Simulation of rapid expansion of supercritical fluid flow. *Eur J Mech B/ Fluids*. 1996;15:569–596.
17. Roe PL. Approximate Riemann solvers, parameter vectors, and difference schemes. *J Comput Phys*. 1981;43:357–372.
18. Moussa AB, Ksibi H, Tenaud C, Baccar M. Parametric study on the nozzle geometry to control the supercritical fluid expansion. *Int J Therm Sci*. 2005;44:774–786.
19. Moussa AB, Ksibi H, Baccar M. Simulation of particles transport and coagulation during the RESS process. *Eur Phys J Appl Phys*. 2008;43:253–261.
20. Franklin RK, Edwards JR, Chernyak Y, Gould RD, Henon F, Carbonell RG. Formation of perfluoropolyether coatings by the rapid expansion of supercritical solutions (RESS) process. Part 2: numerical modeling. *Ind Eng Chem Res*. 2001;40:6127–6139.
21. Khalil I, Miller DR. The structure of supercritical fluid free-jet expansions. *AIChE J*. 2004;50:2697–2704.
22. Sandler SI. *Chemical, Biochemical, and Engineering Thermodynamics*. USA: Wiley, 2006.
23. Star AM, Edwards JR. Numerical simulation of injection of supercritical ethylene into nitrogen. *J Propulsion Power*. 2006;22:809–819.
24. Silvia DD, Graziani D, Miller DR, Continetti RE. Growth of magnetic thin films using CO_2 RESS expansions. *J Supercrit Fluids*. 2007;42:410–418.
25. Yamamoto S, Matsuzawa R, Furusawa T. Simulation of thermophysical flow in axisymmetric nozzle with expansion chamber. *AIChE J*. 2010;57:2629–2635.
26. Yamamoto S, Furusawa T, Matsuzawa R. Numerical simulation of supercritical carbon dioxide flows across critical point. *Int J Heat Mass Transfer*. 2011;54:774–782.
27. van der Waals JD. *Verh.-K. Ned. Akad. Wet, Afd. Natuurkd., Eerste Reeks*. 1893;1:56.
28. Rowlinson JS. Translation of J. D. van der Waals, The thermodynamic theory of capillary under the hypothesis of a continuous variation of density. *J Stat Phys*. 1979;20:197–244.
29. Cahn JW, Hilliard JE. Free energy of a nonuniform system. III., Nucleation in a two-component incompressible fluid. *J Chem Phys*. 1959;31:688–699.
30. Onuki A. Dynamic van der Waals theory. *Physical Review E* 2007; 75:036304.
31. Xu X, Qian T. Contact line motion in confined liquid-gas systems: slip versus phase transition. *The Journal of chemical physics* 2010; 133:204704.
32. Laurila T, Carlson A, Tapio A, Do-Quang M, Amberg G. Thermohydrodynamics of boiling in a van der Waals fluid. *Physical Review E* 2012;85:026320.
33. Platzer B, Maurer G. A generalized equation of state for polar and nonpolar fluids. *Fluid Phase Equilib*. 1989;51:223–236.
34. Crist S, Sherman PM, Glass DR. Study of highly underexpanded sonic jet. *AIAA J*. 1966;4:68–71.
35. Hatanaka K, Saito T. Influence of nozzle geometry on underexpanded axisymmetric free jet characteristics. *Shock Waves*. 2012;22: 427–434.
36. Mora JF, Hering SV, Rao N, McMurry PH. Hypersonic impaction of ultrafine particles. *J Aerosol Sci*. 1990;21:169–187.
37. Zarea A, Aboualia O, Ahmadib G. Computational investigation of airflow, shock wave and nano-particle separation in supersonic and hypersonic impactors. *J Aerosol Sci*. 2007;38:1015–1030.
38. Anderson DM, McFadden GB, Wheeler AA. Diffuse interface methods in fluid mechanics. *Annu Rev Fluid Mech*. 1998;30:139–165.
39. Wendt JF. *Computational Fluid Dynamics*. Springer-Verlag Berlin Heidelberg, 2009.
40. Span R, Wagner W. A new equation of state for carbon dioxide covering the fluid region from the triple-point temperature to 1100 K at pressures up to 800 MPa. *J Phys Chem Ref Data*. 1996;25:1509.
41. Türk M, Hils P, Helfgen B, Schaber K, Martin H-J, Wahl MA. Micronization of pharmaceutical substances by the rapid expansion of supercritical solutions (RESS): a promising method to improve bioavailability of poorly soluble pharmaceutical agents. *J Supercrit Fluids*. 2002;22:75–84.
42. Amberg G, Tönhardt R, Winkler C. Finite Element simulations using symbolic computing. *Math Comput Simul*. 1999;49:257–274.
43. Do-Quang M, Villanueva W, Loginova I, Amberg G. Parallel adaptive computation of some time-dependent materials-related microstructural problems. *Bull Pol Acad Sci*. 2007;55:229–237.
44. Zienkiewicz OC, Taylor RL, Nithiarasu P. *The Finite Element Method for Fluid Dynamics*. Burlington, MA: Elsevier Butterworth-Heinemann, 01803. 2005.
45. Morgan K, Peraire J, Peiro J, Zienkiewicz OC. Adaptive remeshing applied to the solution of a shock interaction problem on a cylindrical leading edge.In: Stow P. editor. Comput Methods Aeronautical Fluid Dynamics, Oxford: Clarenden Press, 1990:327–344.
46. Vesovic V, Wakeham WA, Olchowy GA, Sengers JV, Watson JTR, Millat J. The transport properties of carbon dioxide. *J Phys Chem Ref Data*. 1990;19:763–808.

Manuscript received June 4, 2014, and revision received Aug. 9, 2014.